# Synergistic Study on Aerodynamic Performance Optimization and Flutter Suppression of a Compressor Impeller Based on Response Surface Method

Zhiqiang Dong, Genliang Yu

Abstract-Hydrogen-fuel-cell air compressors operating at high speed and pressure ratio demand both superior impeller aerodynamics and robust flow-field stability to accommodate the low load capacity and limited stability of gas bearings. In this work, a coupled optimization framework combining aerodynamic efficiency enhancement with flutter suppression is developed using Response Surface Methodology (RSM). A nonlinear surrogate model relating key geometric parameters (tip-clearance ratio, leading-edge angle, trailing-edge angle) to performance metrics (isentropic efficiency, aerodynamic work) established via systematic design-of-experiments. Multi-objective RSM-based optimization then identifies a balanced design that maximizes efficiency while driving overall aerodynamic work from positive to negative, thereby reducing aeroelastic excitation. High-fidelity simulations of the optimized impeller demonstrate a 2.2 % increase in efficiency and a shift to -0.00102 J aerodynamic work per blade, yielding a positive damping coefficient of 0.00078. These results confirm that the proposed methodology effectively enhances compressor performance and suppresses flutter risk, offering valuable guidance for the aeroelastic design of high-speed centrifugal impellers.

Index Terms—Hydrogen Fuel Cell; Centrifugal Compressor; Flutter; Response Surface Optimization

#### I. INTRODUCTION

ITH the rapid development of the new energy vehicle industry, hydrogen fuel cell systems impose increasingly stringent requirements on centrifugal compressors. These systems demand a highly stable air supply in both pressure and mass flow rate, necessitating compressors to operate efficiently and reliably under elevated rotational speeds and pressure ratios[1-3]. Simultaneously, road-induced vibrations introduce severe constraints on the stability and load capacity of gas bearings, highlighting the importance of rotor dynamic balance and high-precision manufacturing[4,5]. As a result, impeller design must simultaneously achieve high aerodynamic efficiency and

Manuscript received May 10, 2025. revised September 9, 2025.

This work was supported by the Shanxi Provincial Basic Research Program (No. 2022203021221152).

Zhiqiang Dong is an Associate Professor at the School of Vehicle and Transportation Engineering, Taiyuan University of Science and Technology, Taiyuan, Shanxi 030024, China (corresponding author to provide phone: +86-18335149923; E-mail: dongzhiqiang@tyust.edu.cn).

Genliang Yu is a Master's student at the School of Vehicle and Transportation Engineering, Taiyuan University of Science and Technology, Taiyuan, Shanxi 030024, China (E-mail: 1981474730@qq.com).

strict manufacturing tolerances. Under extreme conditions, complex internal flow interactions coupled with structural vibrations may trigger flutter—a hazardous form of aeroelastic instability that threatens compressor reliability [6-8]. Therefore, an integrated optimization of aerodynamic and structural characteristics is essential to enhance compressor performance while mitigating flutter risks.

Extensive research has been conducted globally on the aerodynamic and flutter behavior of compressor blades. Early methods evolved from empirical models to high-fidelity simulations combining theoretical frameworks and experimental validation. For instance, John[9] experimentally identified flutter as an aeroelastic phenomenon, linking vortex shedding on the pressure side of blades to excitation of the first bending mode. Vedeneev [10] and Arshad [11] employed the energy method to quantitatively assess flutter risks, demonstrating that flutter occurs when aerodynamic energy input exceeds the mechanical damping capacity. These studies laid a solid theoretical foundation for modern flutter prediction.

Meanwhile, tip clearance effects on compressor performance have attracted considerable attention. Studies by Lakshminarayana [12] and Xin Jian [13] identified strong empirical correlations between tip clearance and key performance metrics, such as efficiency, pressure ratio, and stall margin. Guo-Rong Gao et al. [14]demonstrated that aerodynamic performance deteriorates progressively with increasing tip clearance. Additionally, Zhiyuan Liu [15] and Chenkai Zhang [16] validated through experiments and numerical simulations, respectively, that tip clearance affects leakage flow and flow separation, emphasizing that reducing tip clearance can help improve flow field structure, reduce flow losses, and enhance overall performance.

In terms of flutter prediction, Micklow [17] proposed semi-empirical and semi-theoretical models, including the semi-actuator disk model, which simplified internal flow details while considering inlet and outlet flow characteristics, enabling preliminary flutter risk prediction. Kangdi Li et al. [18]introduced an efficient fluid-structure interaction (FSI) method combining rapid mesh deformation techniques with dual-passage shape correction to predict blade flutter under traveling wave modes. Yupeng Liu et al. [19]developed a multi-physics prediction and flutter characteristics identification method based on deep learning for blade flutter caused by unsteady fluid-structure interaction in compressors. They constructed an end-to-end prediction system linking

design variables of swept blades to three-dimensional physical field parameters on blade surfaces and finally to flutter characteristics. Similarly, Yuxin Gai et al. [20]proposed a time-domain method to analyze aeroelastic stability of wind turbine blades by solving their dynamic response over time to obtain flutter characteristics. Liping Dai et al. [21] predicted the critical flutter wind speed of the NREL 5 MW wind turbine during braking and operating conditions using FAST software based on Blade Element Momentum Theory and a nonlinear geometrically exact beam model, analyzing both structural dynamic response and aerodynamic performance before and after flutter onset. Furthermore, several studies [22-25] have investigated the influence of shock waves, leakage flows, and flow separation near the blade leading edge on aerodynamic damping and flutter characteristics, thus deepening the understanding of aeroelastic instability mechanisms.

Despite the robust theoretical groundwork laid by prior research, several critical challenges persist:

- (1) Limitations of prediction methods: Existing empirical and semi-theoretical models generally rely on extensive experimental data, making them difficult to apply to the design of new high-load, high-pressure-ratio compressors. Furthermore, their descriptions of unsteady phenomena such as shock waves, leakage flows, and localized energy transfer remain inadequate.
- (2) Lack of numerical simulation and multi-objective optimization: Although numerical simulation techniques have significantly advanced in recent years, achieving coordinated optimization of multiple design variables—such as TC/H, leading-edge bending angle ( $\beta_1$ )—in high-speed compressor blade design remains a major challenge. Current studies largely focus on the local effects of individual parameters, lacking systematic investigation into multi-parameter interactions.

To address these issues, this paper proposes an integrated research methodology based on response surface multi-objective optimization. First, using a traveling wave model and the energy method, the role of inter-blade phase angle in flutter onset is quantitatively analyzed from the perspectives of aerodynamic work and damping. Then, by employing a transient blade row model, high-fidelity numerical simulations are conducted to capture shock waves and localized unsteady effects induced by tip clearance. Taking TC/H,  $\beta_1$ , and  $\beta_2$  as design variables, a nonlinear mapping relationship and a TC/H- $\beta_1$ - $\beta_2$  design space are constructed, enabling coordinated optimization between compressor efficiency improvement and aerodynamic work reduction.

#### II. BLADE FLUTTER PREDICTION METHODS

#### A. Energy Method and Damping Characteristics

Flutter is a typical manifestation of fluid-structure interaction, arising from an energy exchange between unsteady aerodynamic forces and structural vibrations. When the energy imparted by the airflow exceeds the intrinsic damping capacity of the structure, the vibration amplitude increases progressively, potentially leading to structural instability or failure.

In centrifugal compressors, adjacent blades often exhibit collective vibration behavior due to aerodynamic coupling. This phenomenon is commonly modeled using the *traveling wave* (or *Lane*) model[26], which assumes that all blades vibrate with the same frequency and amplitude, but with a constant phase shift between adjacent blades. This phase shift is referred to as the Inter-Blade Phase Angle (IBPA), a critical parameter in flutter analysis. Depending on the wave propagation direction relative to rotor rotation, traveling waves are categorized into forward (0° < IBPA < 180°) and backward ( $-180^{\circ}$  < IBPA < 0°) modes.

In this study, the centrifugal impeller is designed with 20 blades. The relationship between IBPA and blade count is defined by Equation (1):

$$IPBA = \frac{2\pi \cdot N_D}{N_R} \tag{1}$$

Where:  $N_B$  denotes the number of blades, and  $N_D$  represents the number of pitch wise divisions. When the number of blades is even,  $0 \le N_D \le N_B/2$ . When the number of blades is odd,  $0 \le N_D \le (N_B - 1)/2$ .

To assess flutter risk, the energy method is frequently employed. It evaluates the net aerodynamic work WWW done on the blade surface over one vibration cycle, as shown in Equation (2). A positive accumulated work indicates that the blade extracts energy from the flow, potentially causing flutter. In contrast, a negative value reflects energy dissipation, thereby promoting aeroelastic stability.

$$W = \int (p\vec{n})\vec{V}_g dS \tag{2}$$

Where: W is the aerodynamic work, p is the static pressure on the blade surface,  $\vec{n}$  is the unit outward normal vector at a point on the blade surface, S is the blade surface area.

A dimensionless parameter used to quantify the influence of airflow on blade vibration is the aerodynamic damping ratio, defined as in Equation (3). A positive aerodynamic damping ratio indicates that the airflow acts as a damping force, whereas a negative value suggests that the flow excites the blade, increasing the risk of flutter.

$$\xi = \frac{-W}{\rho \cdot \omega^2 \cdot \int (A_x^2) dV}$$
 (3)

Where:  $\rho$  is the blade material density,  $\omega$  is the angular frequency of blade vibration, A is the vibration amplitude at a given point.

#### B. Transient Blade Row (TBR) Model

The Transient Blade Row (TBR) model is an unsteady numerical approach designed to capture the dynamic flow behavior around rotating blades. Unlike steady-state solvers, the TBR method resolves the governing equations in the time domain, enabling detailed analysis of unsteady phenomena such as flutter, aerodynamic damping, and leakage vortex-induced nonlinearities.

The TBR model solves governing equations in the time domain to obtain transient distributions of flow field parameters such as pressure and velocity. Its core methodologies include: Transient flow field decoupling, allowing local unsteady analysis on periodically arranged blades to reduce computational cost; Extraction of unsteady

aerodynamic loads, capturing time-dependent aerodynamic forces from blade surface pressure distributions; Fluid–structure interaction (FSI) analysis, where blade modal characteristics are coupled with the unsteady flow to evaluate flutter risk.

#### III. NUMERICAL MODEL

#### A. Numerical Model of the Centrifugal Compressor

To optimize rotor dynamic performance and facilitate manufacturing, a semi-open, single-stage centrifugal impeller with 20 blades was selected for this study. The initial geometric and aerodynamic design parameters are summarized in Table I, and the corresponding three-dimensional CAD model is presented in Fig. 1.

TABLE I INITIAL DESIGN PARAMETERS

Symbol	Parameter	Value	
$d_{\scriptscriptstyle H}$	Inlet hub diameter	100 mm	
$d_{\scriptscriptstyle S}$	Inlet shroud diameter	180 mm	
	TC/H	0.05	
n	Design rotational speed	40000 r/min	
P	Design pressure ratio	4.5	
m	Design mass flow rate	3 kg/s	

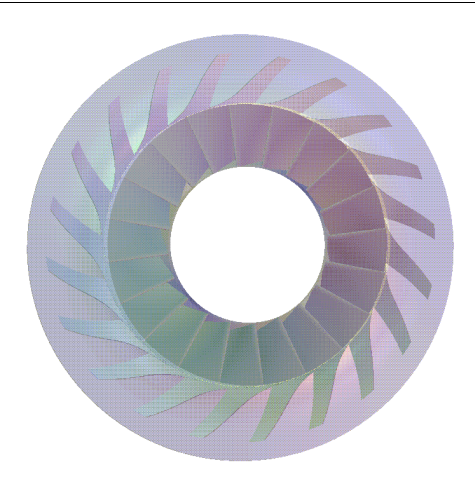


Fig. 1. Impeller 3D model

#### B. Mesh Generation

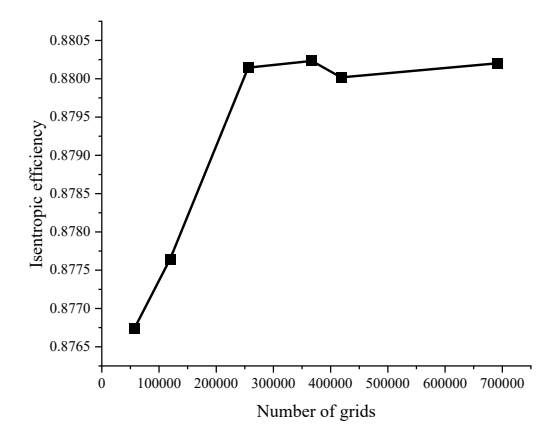
To balance numerical accuracy and computational efficiency, mesh generation was carried out using ANSYS Turbo Grid, a specialized meshing tool for turbomachinery applications. A single flow passage was modeled under periodic boundary conditions, which is a widely accepted practice in rotating machinery simulation.

Turbo Grid generates high-quality structured meshes and is well-suited for complex blade geometries. An O4H mesh topology was adopted to ensure accurate resolution of boundary layer effects and tip-leakage vortices. Local mesh refinement was applied along the blade surfaces and in the tip clearance region to capture critical flow features. The final mesh topology is illustrated in Fig. 2.

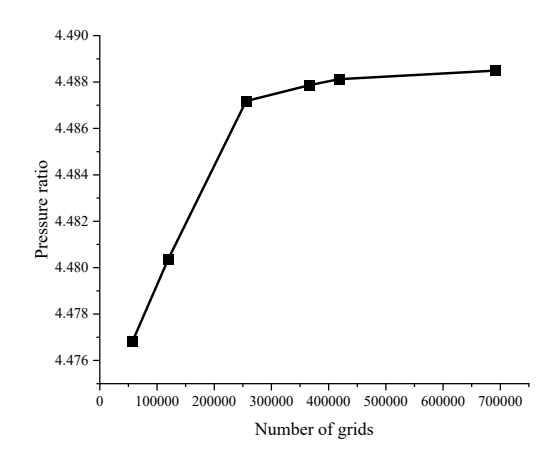


Fig. 2. Impeller structure grid

To validate the influence of mesh density on the simulation results, a grid independence study was conducted. The isentropic efficiency and total pressure ratio of the impeller were used as performance indicators to assess sensitivity to mesh resolution. As shown in Fig. 3, when the number of grid elements in a single flow passage exceeds 250,000, the simulation results show minimal variation. Therefore, to balance accuracy and computational cost, the mesh configuration adopted in this study includes 255,891 elements and 278,372 nodes.



#### (a) Isentropic efficiency



(b) Pressure ratio
Fig. 3. Grid independence verification

#### C. Boundary Conditions

In numerical simulations, proper specification of boundary conditions is essential to ensure the reliability of results. In this study, pressure inlet and pressure outlet boundary conditions were applied at the impeller's inlet and outlet, respectively. The initial total temperature and total pressure of the incoming flow were set to 288.15 K and 101.325 kPa, respectively. No-slip boundary conditions were imposed on both the impeller surfaces and the tip clearance region.

The impeller rotational speed was set to 40,000 rpm, and the Multiple Reference Frame (MRF) method was employed to handle the coupling between the rotating and stationary domains. The Shear Stress Transport (SST) turbulence model was used in conjunction with the TBR model to capture complex turbulence features and unsteady aerodynamic loads.

## IV. BLADE FLUTTER CHARACTERISTICS ANALYSIS AND DESIGN SPACE DEFINITION

This section investigates the influence of key geometric and operating parameters on impeller performance and stability through modal analysis, steady-state simulations, and unsteady aeroelastic evaluation. These results form the basis for subsequent response surface-based design optimization.

#### A. Structural Dynamics Simulation of the Blade

Structural dynamic modeling is fundamental in analyzing

TABLE II

blade flutter characteristics. In this study, the finite element method (FEM) was used to establish the structural model of the impeller blade, with titanium alloy as the material. The material properties are listed in Table II. The mesh was composed of Solid186 second-order tetrahedral elements, which offer high accuracy in capturing complex 3D stress fields

To simplify the simulation while maintaining result fidelity, the blade root was fully constrained, a common conservative assumption in engineering practice. A gravitational field was applied in the negative X-direction to account for self-weight deformation, and a rotational load of 40,000 rpm was imposed around the negative Z-axis.

Modal frequencies were computed for the first six natural modes under both pure centrifugal loading and combined centrifugal–aerodynamic loading, across various tip clearance-to-span (TC/H) ratios. The results, presented in Table III, show that natural frequencies increase with TC/H. Under centrifugal loads alone, frequency increases by 3.3% to 5.0% as TC/H increases from 0.01 to 0.10, particularly in higher modes due to their greater sensitivity to stiffness variation and stronger bending–torsion coupling.

The introduction of aerodynamic loads causes only minor frequency shifts, indicating limited stiffness influence. However, torsional effects are amplified, especially in higher-order modes, due to inter-span pressure gradients and increased blade twist under aerodynamic forcing.

BLADE MATERIAL PROPERTIES				
Density (kg/m³)	Elastic Modulus (MPa)	Poisson's Ratio	Yield Strength (MPa)	
4620	96000	0.36	930	

Density (kg/m²)		Elastic Modulus (MFa)		Foisson's Ratio		Held Strength (MPa)	
4620		96000		0.36		930	
	TABLE III Modal Frequencies of the First Six Modes Under Different TC/H Ratios and Load Conditions						
TC/H	Load Type	1st Mode	2nd Mode	3rd Mode	4th Mode	5th Mode	6th Mode
		(Hz)	(Hz)	(Hz)	(Hz)	(Hz)	(Hz)
0.01	Centrifugal	2513.5	4835.2	6220.5	7254.3	7912.3	9016.4
0.01	Centrifugal + Aero	2511.7	4833.3	6218.6	7247.6	7900.5	9003.7
0.03	Centrifugal	2531.5	4870.2	6277.1	7322	7986.6	9113.4
0.03	Centrifugal + Aero	2531.7	4874.4	6282.3	7325.3	7991.8	9120.1
0.05	Centrifugal	2550.4	4909.3	6335.9	7392.6	8069.7	9216.4
0.03	Centrifugal + Aero	2550.4	4910.5	6337.6	7393.3	8069.2	9214.1
0.07	Centrifugal	2569	4944.7	6391.7	7460.6	8143.9	9314.1
0.07	Centrifugal + Aero	2568.7	4944.4	6389.8	7458.5	8141.5	9308.5
0.09	Centrifugal	2586.7	4977.7	6448.7	7531.7	8218.7	9413.3
0.09	Centrifugal + Aero	2588.4	4983.8	6453	7539.3	8231.8	9424.3
0.1	Centrifugal	2597.1	4999.8	6478.3	7567.9	8259.7	9467.9
0.1	Centrifugal + Aero	2597.5	4999.9	6482	7577.3	8270.8	9475.5

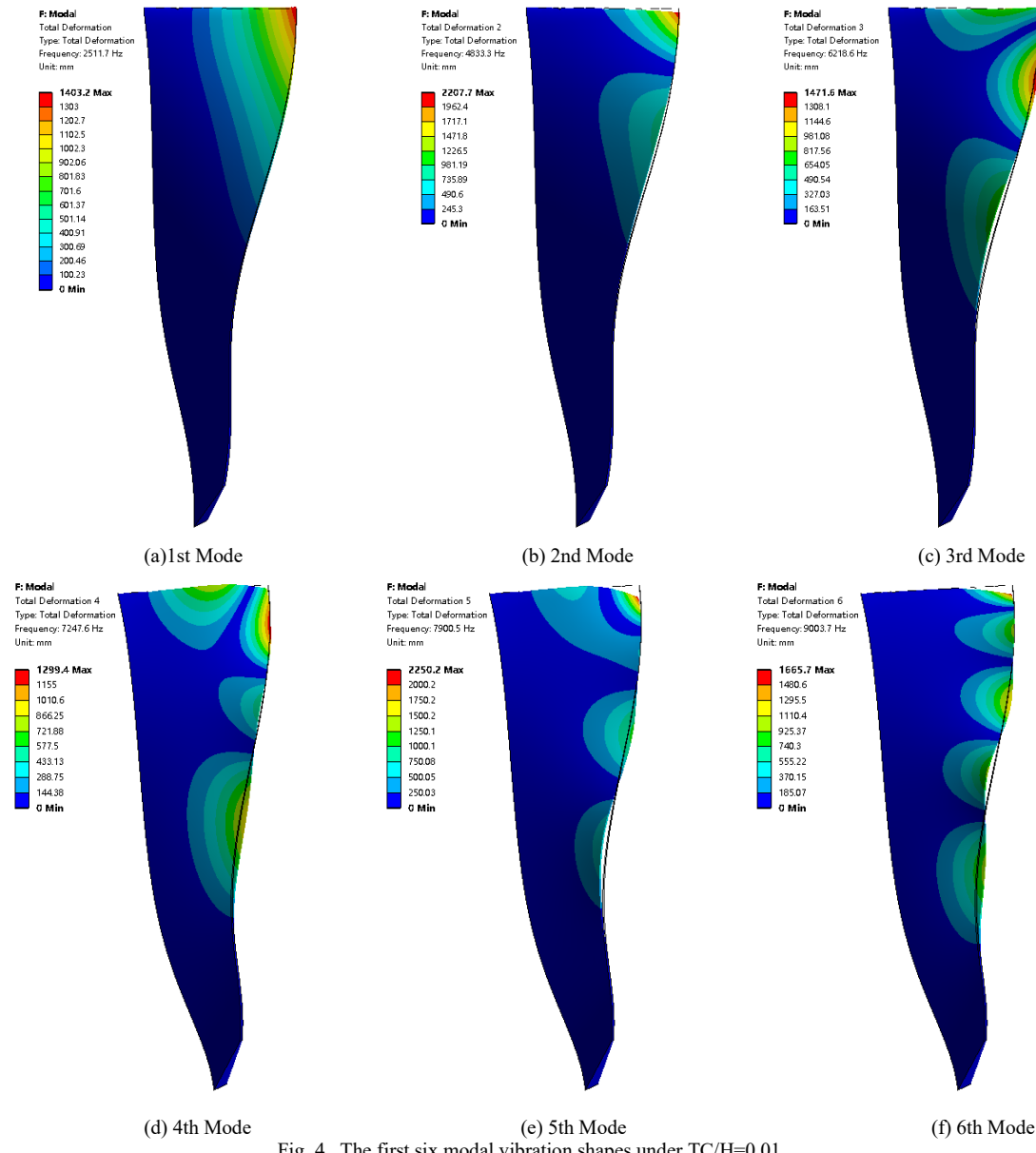


Fig. 4. The first six modal vibration shapes under TC/H=0.01

The blade vibration modes for various TC/H values ranging from 0.01 to 0.1 exhibit consistent deformation trends, with only minor differences in the vertical distribution of the displacement amplitude. Therefore, only the representative mode shapes for TC/H = 0.01 are illustrated in Fig.4.As observed, the first six vibration modes progressively transition from bending-dominated to torsion-dominated behaviors, revealing increasing structural complexity with mode order:

(a)1st Mode: Characterized primarily by spanwise bending, with displacement gradually increasing from the root to the tip and peaking at the tip. The overall deformation is relatively simple, indicating dominant influence from bending stiffness at low frequencies.

(b)2nd Mode: Onset of bending-torsion coupling. While bending remains dominant, local torsional deformation begins to emerge, suggesting increasing sensitivity to torsional stiffness at this mode order.

(c)3rd Mode: Torsional effects become more pronounced. Significant relative twist between blade sections indicates a transition from bending-dominated to torsion-dominated deformation, with torsional stiffness playing a critical role in shaping the mode.

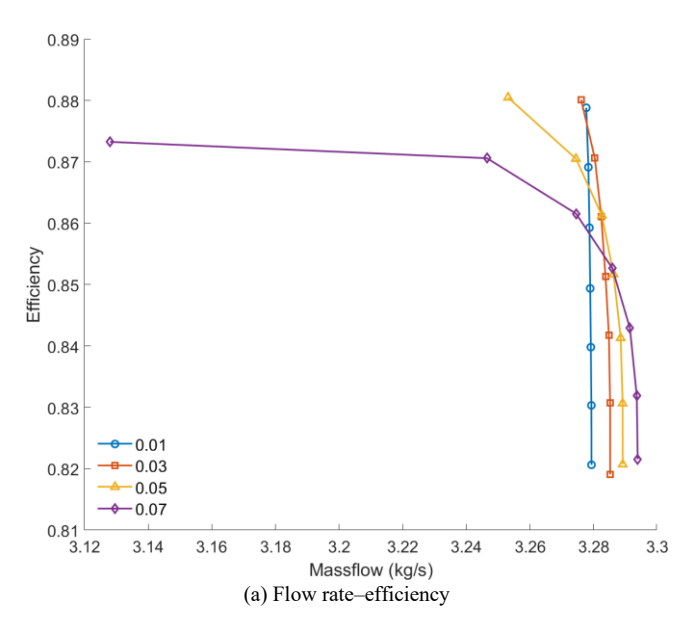
(d)4th Mode: Stronger bending-torsion coupling is evident. Multiple bending nodes appear along the span, and torsional deformation is localized in specific regions. The peak displacement is no longer confined to the tip but distributed across different blade heights.

(e)5th Mode: Deformation becomes increasingly complex, with enhanced relative twist between sections and multiple regions exhibiting concentrated torsion. Compared to the fourth mode, the dominance of torsional stiffness becomes more apparent.

(f)6th Mode: The deformation is now overwhelmingly torsion-dominated. Relative angular displacement between adjacent sections is significant, and bending effects are substantially diminished. The mode reflects the highest reliance on torsional stiffness under high-order vibration conditions.

The blade has undergone various modal analyses, including prestressed modal analysis that accounts for aerodynamic forces. In energy-based flutter prediction methods, the modes with potential flutter risks are typically selected for detailed analysis—most commonly the first bending mode or a torsional mode. Therefore, the first bending mode is selected below as the critical mode for focused investigation.

### B. Steady-State Flow Characteristics and Design Variable Selection



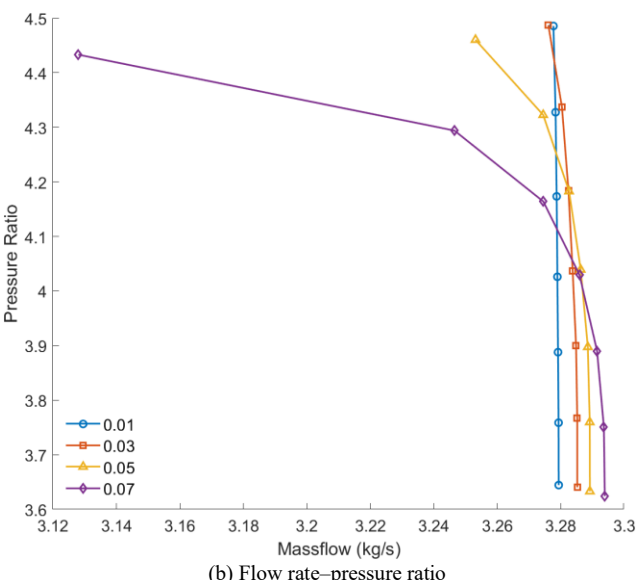


Fig. 5. Impeller characteristic curves at different ratios

Prior to unsteady analysis, steady-state CFD simulations were conducted to assess baseline flow field behavior and identify sensitive design variables. Performance curves under various TC/H ratios are plotted in Fig. 5.

When TC/H exceeds 0.07 (e.g., at TC/H = 0.09 and 0.1), the interaction between tip leakage flow and end wall boundary layers becomes significantly intensified, leading to compressor stall before reaching the design pressure ratio. Therefore, in order to accurately capture the nonlinear influence mechanism of the clearance parameter on compressor performance, only cases within the TC/H range of 0.01 to 0.07 are selected for comparative analysis in the performance curves.

As shown in Fig. 5, with TC/H increasing from 0.01 to 0.07, the flow rate under near-choking conditions gradually decreases. This is primarily due to the enhanced leakage flow

caused by increased tip clearance, and the intensification of tip leakage vortices leads to aggravated secondary flow losses. Consequently, the effective flow area decreases, and flow field distortion and separation in the main flow region are induced. Comparative analysis reveals that cases with TC/H = 0.03 and 0.05 exhibit superior overall performance, with their isentropic efficiencies improved by 0.13% and 0.19%, respectively, compared to the baseline case (TC/H = 0.01).

#### C. Aerodynamic Damping and Flutter Sensitivity Analysis

The inter-blade phase angle (IBPA) is a key parameter affecting the aeroelastic stability of blades. As shown in Fig. 6, for the first-order bending mode, the influence of IBPA on the aerodynamic damping coefficient was analyzed under different TC/H ratios. The least stable conditions are consistently observed near IBPA = 15°. The results show that under various clearance ratios, the aerodynamic damping coefficient exhibits a quasi-sinusoidal variation with IBPA. For TC/H values ranging from 0.01 to 0.09, the aerodynamic damping coefficients remain positive, indicating good aerodynamic stability and effective suppression of flutter risks within this range. However, when TC/H increases to 0.1, negative values of the damping coefficient appear at certain phase angles, suggesting that the blade enters an aeroelasticly unstable regime, with a higher risk of flutter instability.

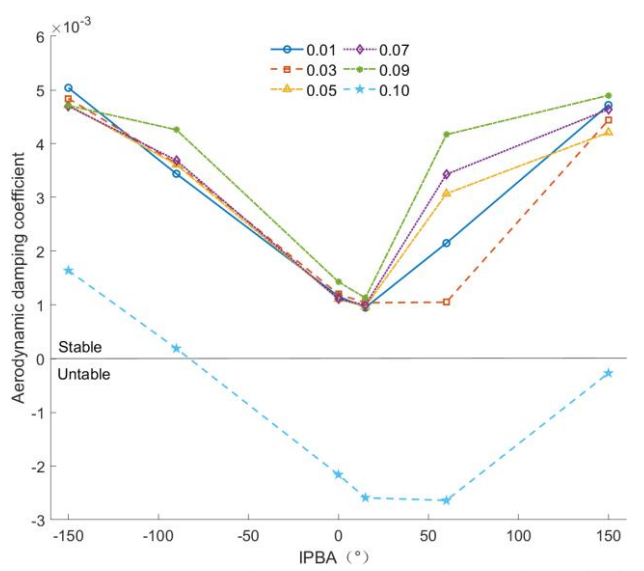


Fig. 6. Variation of aerodynamic damping coefficient with inter-blade phase angle

As shown in Fig. 7, the tip clearance—to—span ratio (TC/H) exerts a more pronounced influence on the blade's suction surface, particularly in the leading-edge region along the chord. As TC/H increases, the positive peak of accumulated work density at the suction-side leading edge rises markedly, revealing that the aerodynamic work input from the flow intensifies significantly. This elevation in work density correlates directly with a heightened risk of aeroelastic instability in this region. On the pressure surface, by contrast, regions of elevated instability risk concentrate toward the trailing edge. With larger clearances, the area over which the accumulated work density is positive expands, demonstrating that variations in TC/H adversely affect aerodynamic stability on both blade surfaces.

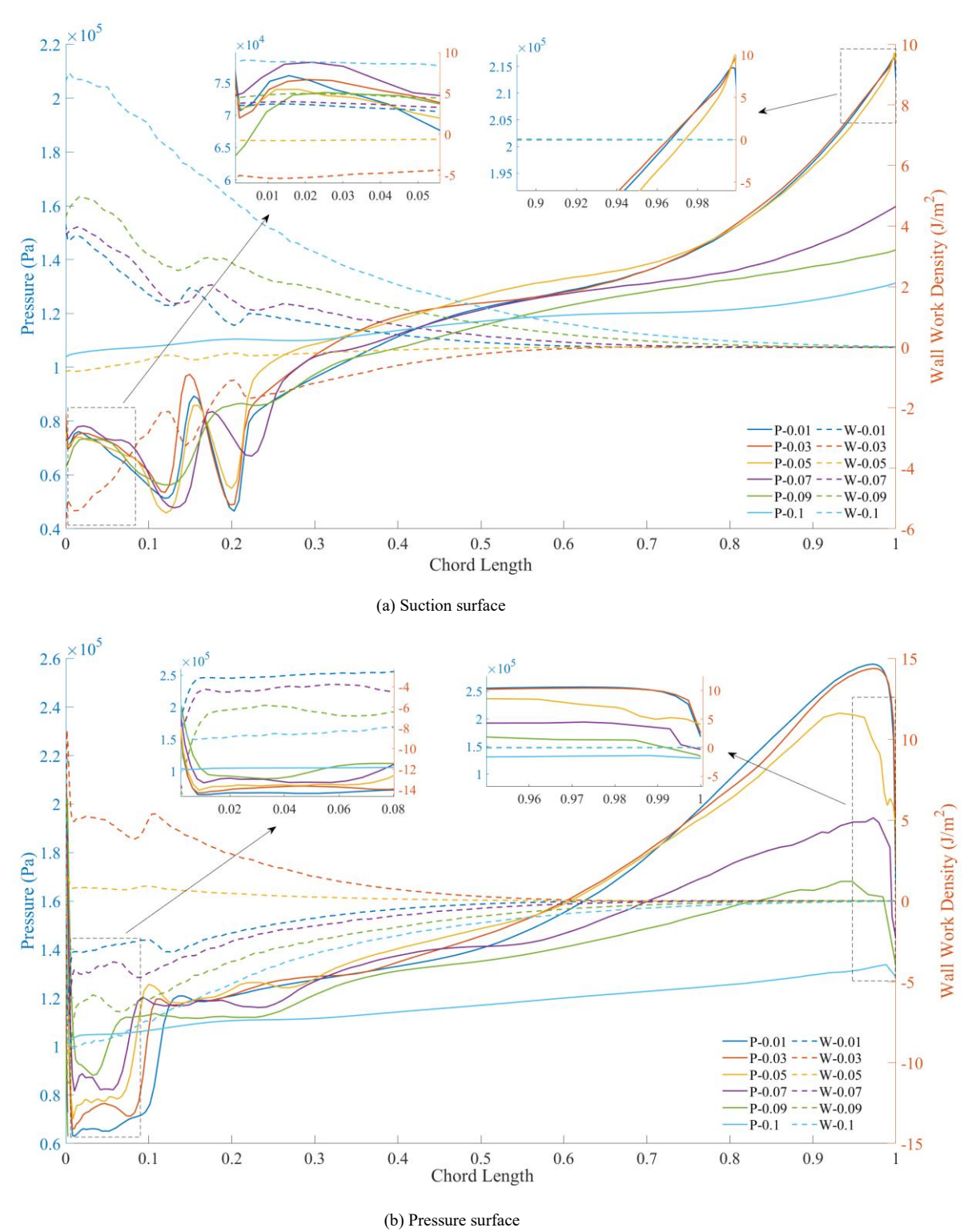


Fig. 7. Distribution of pressure and accumulated work density along the chord length at 95% blade height

Examining the static pressure distribution curves presented in Fig. 7(a), a distinct and rapid pressure rise is observed between 10 % and 40 % of the chord length, which is a classical indicator of shock-induced compression in transonic blade flows. This feature strongly suggests that, on the suction surface of the blade, shock waves are prone to form within the chordwise interval of 0.1–0.4. As the tip clearance-to-vane height ratio (TC/H) increases, the foot of the shock is found to migrate slightly downstream, implying that larger tip clearance delays the onset of shock formation and modifies the local loading distribution along the suction

surface. In contrast, the shock phenomena on the pressure side appear less pronounced, as this surface predominantly resides in a compressed flow regime and therefore experiences weaker adverse pressure gradients. Nevertheless, Fig. 7(b) reveals the presence of localized pressure spikes within the same chordwise range, indicating that compressive disturbances are still capable of inducing unsteady aerodynamic perturbations even on the pressure surface. When the shock propagates across the blade surface, it generates abrupt fluctuations and even sign reversals in the accumulated aerodynamic work density, particularly on the

suction side. The corresponding work density distributions clearly display strong oscillations within the 0.1–0.4 chord region, thereby confirming that shock-related interactions substantially amplify the local aerodynamic work exchange. Such effects constitute a primary mechanism responsible for the deterioration of aeroelastic stability, as they intensify energy transfer between the unsteady flow and the vibrating blade.

A quantitative evaluation of the aerodynamic work on the blade surface for different TC/H values is provided in Table IV, which reports the total aerodynamic work per blade corresponding to each case.

TABLE IV
THE OVERALL AERODYNAMIC WORK OF THE BLADE UNDER DIFFERENT
CLEARANCE RATIOS

Tip Clearance/Blade Height	Aerodynamic Work (J)		
0.01	-0.000324		
0.03	0.000519		
0.05	0.000102		
0.07	-0.00053		
0.09	-0.00074		
0.1	-0.00022		
0.07 0.09	-0.00053 -0.00074		

The results indicate that in most TC/H cases, the total aerodynamic work on the blade is negative, meaning that during the vibration cycle, the incoming flow does negative work on the blade, resulting in energy dissipation that suppresses flutter and enhances aeroelastic stability. However, for the TC/H = 0.03 and TC/H = 0.05 conditions, the total aerodynamic work is 5.18584×10<sup>-4</sup> J and 1.0209×10<sup>-4</sup> J respectively, both of which are positive. This suggests that in these scenarios, the blade absorbs some external energy during vibration. Such energy accumulation may reduce the aerodynamic damping effect, thereby lowering blade stability and increasing the risk of flutter instability. Therefore, to minimize the flutter risk while maintaining aerodynamic performance, further aerodynamic optimization is needed within the TC/H = 0.03-0.05 range to reduce the regions of positive aerodynamic work and enhance overall blade stability.

#### V. OPTIMIZATION MODEL DEVELOPMENT AND VALIDATION

Building upon the critical design variables and sensitive performance indicators identified in Chapter III, this chapter constructs a response surface model, performs multi-objective optimization to determine the optimal parameter set, and visualizes the optimization landscape, followed by validation of the prediction accuracy..

#### A. Response Surface Experimental Design

As indicated by the steady-state flow analysis, the impeller demonstrates superior aerodynamic performance when the tip clearance-to-blade height ratio (TC/H) is maintained within the range of 0.03-0.05. While this interval enhances overall efficiency and improves flow-field uniformity, it simultaneously increases the susceptibility to flutter, which poses a potential threat to aeroelastic stability and long-term structural reliability. To address this intrinsic trade-off between aerodynamic efficiency and flutter resistance, TC/H is considered alongside the leading-edge bending angle  $(\beta_1)$ and trailing-edge bending angle ( $\beta_2$ ) as the principal design variables for optimization, since these parameters exert a first-order influence on leakage losses, flow incidence, diffusion processes, and the aerodynamic load distribution across the blade. For the optimization objectives, impeller efficiency and aerodynamic work are selected, the former reflecting the global energy conversion capability of the compressor stage and the latter quantifying the flow-structure energy exchange that directly governs aerodynamic damping. To establish accurate correlations between the chosen design parameters and performance indicators, a response surface methodology (RSM) is employed, which provides an efficient surrogate modeling framework for capturing nonlinear interactions while reducing computational cost. This approach enables a systematic multi-objective optimization to identify design configurations that reconcile high aerodynamic efficiency with enhanced aeroelastic stability. The distribution of sampling points in the design space and their corresponding high-fidelity numerical simulation results, which serve as the foundation for constructing the response surfaces, are summarized in Table V.

 $TABLE\ V$  Design of Sample Points and Simulation Results for the Response Surface

No.	TC/H	Leading edge bending angle (°)	Trailing edge bending angle (°)	Efficiency	Aerodynamic Work (J)
1	0.045	40	30	0.887207	0.01345
2	0.045	45	35	0.88833	-0.00036
3	0.045	45	35	0.88833	-0.00036
4	0.03	45	30	0.881198	0.0003466
5	0.045	45	35	0.88833	-0.00036
6	0.06	45	30	0.88327	0.00146
7	0.045	40	40	0.73973	-0.00001
8	0.03	40	35	0.87693	0.00284
9	0.045	45	35	0.88833	-0.00036
10	0.06	50	35	0.74482	-0.00227
11	0.06	40	35	0.74287	0.00204
12	0.045	45	35	0.88833	-0.00036
13	0.045	50	40	0.7406	0.00407
14	0.03	45	40	0.88802	-0.00281
15	0.045	50	30	0.85656	-0.00037
16	0.06	45	40	0.66821	-0.0021
17	0.03	50	35	0.86444	-0.00259

#### B. Regression Modeling and Error Evaluation

The Response Surface Methodology (RSM) utilizes polynomial functions to approximate complex nonlinear relationships between design variables and performance responses within a localized design space. By relying on a relatively limited number of high-fidelity sample points and concise algebraic expressions, RSM provides an efficient means of reducing computational cost while preserving sufficient accuracy for optimization purposes. Owing to these advantages, it has been extensively employed in aerodynamic design and multi-objective optimization studies. In the present work, a quadratic multivariate regression model incorporating both linear and interaction terms is adopted to construct the surrogate model, thereby capturing not only the primary effects of the design variables but also their coupled influences on the objective functions. This formulation enables a more accurate representation of the underlying performance trends and provides a reliable analytical foundation for subsequent optimization:

$$y(x) = A_0 + \sum_{i=1}^{n} \alpha_i \beta_j + \sum_{i=1}^{n} \alpha_{ij} x_i^2 + \sum_{i=1}^{n} \alpha_{ij} x_i x_j$$
 (4)

In the equation,  $A_0$  denotes the constant term coefficient, while  $x_i$  represents the design variables at different levels, namely the tip clearance-to-blade height ratio (TC/H), the blade leading-edge bending angle, and the trailing-edge bending angle.

Using the selected design variables as inputs and the impeller efficiency together with the aerodynamic work as response outputs, response surface surrogate models are constructed to approximate the behavior of the objective functions within the defined design space. This surrogate modeling approach enables the capture of nonlinear relationships between the geometric parameters and performance indicators while significantly reducing the computational cost compared with direct high-fidelity simulations. On the basis of the fitted response surfaces, regression equations are derived for both impeller efficiency and aerodynamic work, providing explicit functional expressions that quantitatively describe the influence of the design variables. These regression models serve as the foundation for subsequent optimization, offering an efficient and reliable means to explore the trade-off between aerodynamic performance and aeroelastic stability. The regression equations are expressed as follows:

$$\eta = 0.8883 - 0.0589A - 0.005B - 0.059C + 0.0036AB - 0.0555AC + 0.0079BC - (5) \\
0.0285A^2 - 0.0526B^2 - 0.0297C^2 \\
A_w = -0.0004 - 0.0002A - 0.0024B - 0.0024C + 0.0003AB + 0.0007AC + 0.0045BC - (6) \\
0.0019A^2 + 0.0023B^2 + 0.0023C^2$$

Where variable A denotes the tip clearance-to-blade height ratio (TC/H), B represents the leading-edge bending angle, and C the trailing-edge bending angle.

As shown in Table VI, the regression equations demonstrate excellent fitting performance, with both the coefficient of determination (R<sup>2</sup>) and the adjusted R<sup>2</sup> values being very close to 1. This indicates that the constructed models are capable of accurately capturing the variation

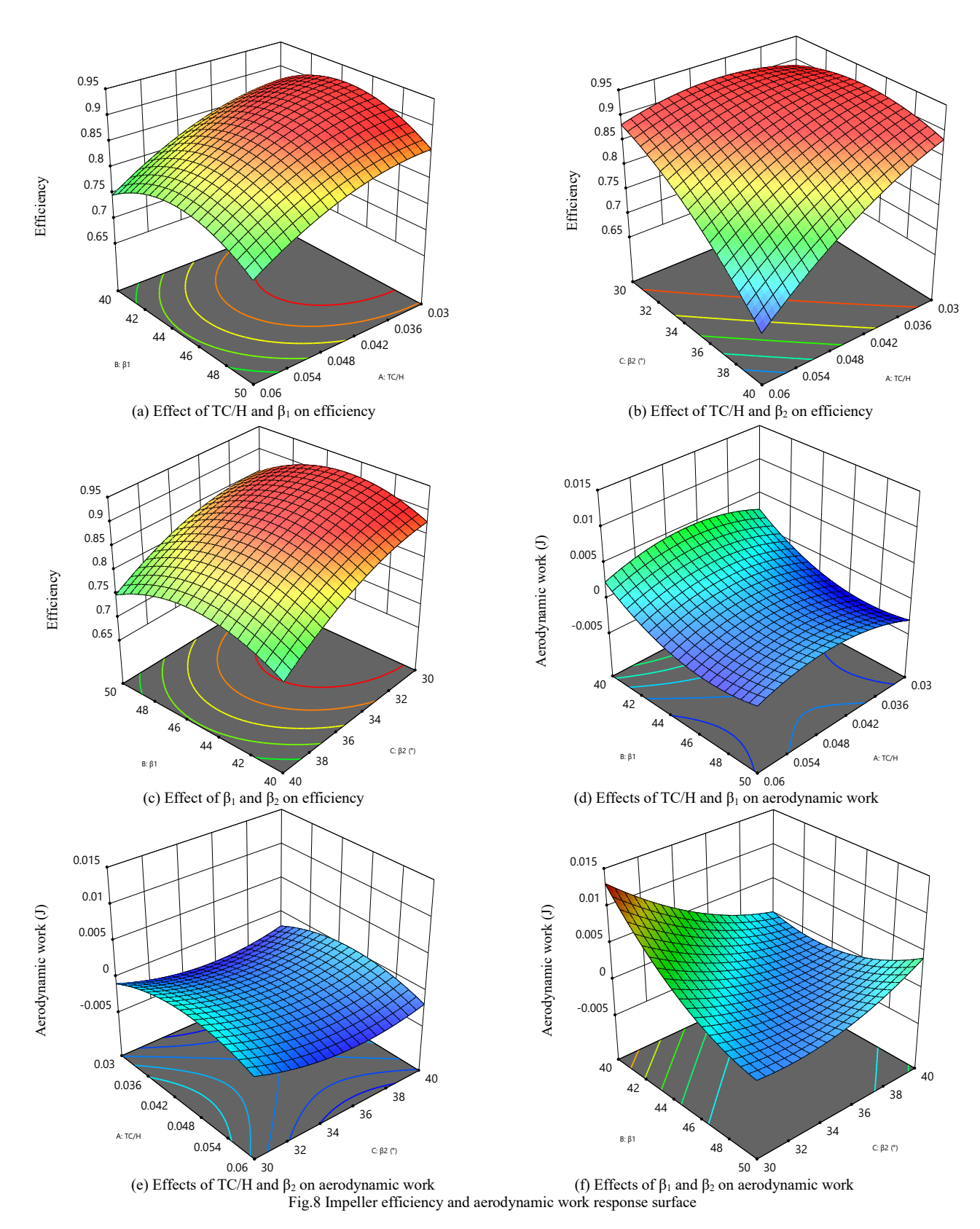
trends in both efficiency and aerodynamic work across the design space. Furthermore, the low standard deviation highlights the minimal degree of data dispersion, confirming that the simulation data are well represented by the fitted regression surfaces. In addition, the predicted R<sup>2</sup> value is also high, which reflects the strong capability of the models to generalize beyond the sampled design points and reliably predict the response behavior for unseen cases. Equally important, the Adequate Precision values are much greater than the critical threshold of 4, suggesting that the models possess a high signal-to-noise ratio. This ensures that the regression equations not only provide statistically significant fits but also offer stable and dependable guidance for subsequent optimization analyses.

TABLE VI REGRESSION EQUATION ERROR STATISTICS

Statistical Index	Efficiency	Aerodynamic Work
Std. Dew.	0.0092	0.0001
Mean	0.8362	0.0009
C.V.%	1.10	16.28
R2	0.9934	0.9994
Adjusted R2	0.9850	0.9985
Predicted R2	0.8950	0.9898
Adep Precision	33.5241	145.8285

### C. Response Surface Analysis of Impeller Efficiency and Aerodynamic Work

The response surface plots fitted from the experimental design data reveal the relationships between key geometric parameters and the performance metrics. Figure 8 illustrates the response surfaces of impeller efficiency and aerodynamic work. Significant interaction effects are observed among the design variables, with pronounced surface curvature indicating strong nonlinear dependencies, underscoring the importance of carefully balancing multiple design factors. For impeller efficiency, Fig. 8(a) shows that efficiency increases and then decreases with the leading-edge bending angle (β<sub>1</sub>), reaching a maximum within 44°–46°, and further improves with increasing TC/H. Fig. 8(b) highlights a similar trend for TC/H, with efficiency rising more noticeably when the trailing-edge bending angle ( $\beta_2$ ) is small but plateauing or slightly declining when β<sub>2</sub> exceeds 35°–40°, indicating limits to the beneficial effect of outlet angle adjustments. Fig. 8(c) confirms that peak efficiency occurs at  $\beta_1 = 44^{\circ}-46^{\circ}$ , with a continuous increase as  $\beta_2$  grows, demonstrating the coupled influence of inlet and outlet bending angles. The trends in aerodynamic work, shown in Fig. 8(d)-(f), exhibit distinct patterns: Fig. 8(d) indicates an initial increase followed by a slight decrease with TC/H, while β<sub>1</sub> exerts a generally negative effect on work. Fig. 8(e) shows a maximum within TC/H = 0.042–0.048, with non-monotonic variations along  $\beta_2$ , and Fig. 8(f) demonstrates that low  $\beta_1$  and  $\beta_2$  values lead to the highest aerodynamic work, implying that smaller inlet and outlet angles enhance energy input but also elevate energy dissipation. Collectively, these observations highlight the intricate trade-offs among geometric configuration, aerodynamic efficiency, and energy transfer, providing insights for guiding multi-objective optimization and improving overall impeller performance under varying design conditions.



#### D. Multi-Objective Optimization

To improve impeller efficiency while suppressing flutter, TC/H,  $\beta_1$ , and  $\beta_2$  are constrained variables. A multi-objective optimization model is established, aiming to maximize efficiency and minimize aerodynamic work (targeting negative values). Since multi-objective problems involve inherently conflicting goals, global optimization within specified variable ranges is necessary to achieve a balanced optimal solution.

Multi-objective optimization model:

$$\max f_{1} = \eta(TC/H, \beta_{1}, \beta_{2}) 
\min f_{2} = A_{w}(TC/H, \beta_{1}, \beta_{2}) 
0.03 \le TC/H \le 0.06 
40 \le \beta_{1} \le 50 
30 \le \beta_{2} \le 40$$
(7)

Where:  $\eta$  denotes impeller efficiency,  $A_w$  represents aerodynamic work.

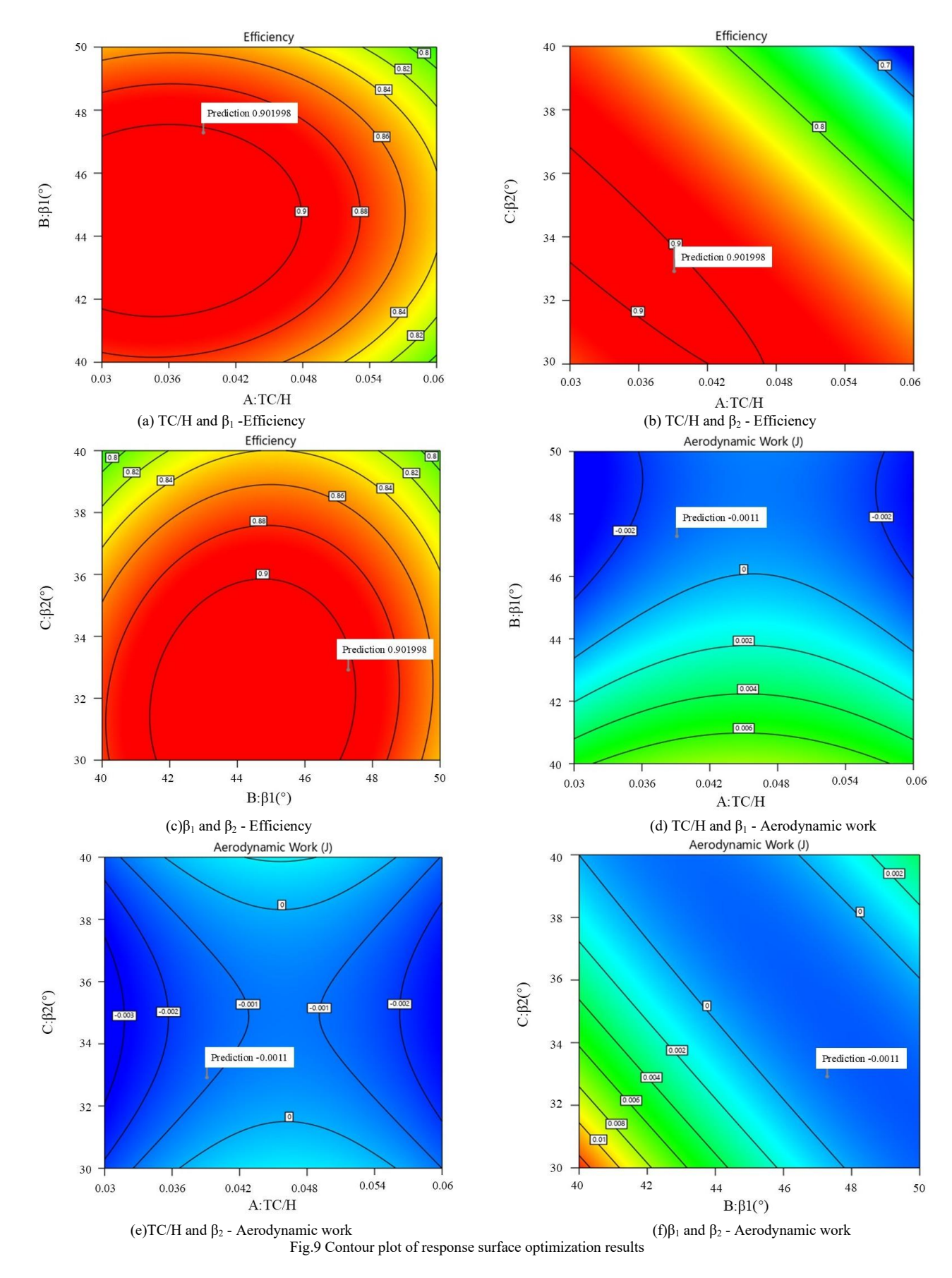


TABLE VII
COMPARISON OF PREDICTED AND SIMULATED VALUES

Type	TC/H	Leading edge bending angle (°)	Trailing edge bending angle (°)	Efficiency	Aerodynamic Work (J)
Predicted	0.039	47.284	32.918	0.902	-0.0011
Simulated	0.039	47.28	32.92	0.900291	-0.00101912

After performing response surface optimization on the above multi-objective functions, the contour plot of the optimization results is obtained as shown in Figure 9. Optimization results indicate that TC/H,  $\beta_1$ , and  $\beta_2$  significantly influence both performance metrics. An optimal combination of moderate TC/H ( $\approx$  0.04), relatively large  $\beta_1$  ( $\approx$  47°), and appropriate  $\beta_2$  ( $\approx$  33°) improves efficiency and reduces flow loss. Excessively large TC/H or  $\beta_2$  increases energy dissipation, while increasing  $\beta_1$  helps reduce aerodynamic work and suppress flutter. The final optimized parameters are TC/H = 0.0391,  $\beta_1$  = 47.28°, and  $\beta_2$  = 32.92°, achieving high efficiency with minimal aerodynamic work, contributing to improved system stability.

To validate the optimization results, the predicted values were compared with the simulation results. As shown in Table VII, the CFX simulation data closely match the predicted values, with an efficiency deviation within 0.189% and an aerodynamic work deviation within 7.35%. This high level of agreement confirms the predictive accuracy and reliability of the response surface optimization method.

#### E. Analysis of Optimization Results

(1) Comparison of Blade Geometry Before and After Optimization

As illustrated in Fig. 10, the optimized impeller exhibits a slight geometric modification, with the leading-edge bending angle increased by 0.44° and the trailing-edge bending angle reduced by 2.08°. These adjustments contribute to a more favorable flow guidance and redistribution of aerodynamic loading along the blade span.

Fig. 11 further compares the external performance characteristics of the impeller before and after optimization. Both models present similar overall performance trends, where efficiency decreases gradually as the mass flow rate increases. However, the optimized impeller demonstrates clear performance gains, with efficiency improvements of 2.24% at TC/H = 0.03 and 2.2% at TC/H = 0.05. Importantly, these enhancements are achieved without sacrificing the pressure ratio, which remains essentially unchanged, thereby confirming that the optimization effectively enhances compressor efficiency while maintaining stable pressure rise capability.

As shown in Fig.12, aerodynamic work is mainly concentrated near the leading edge, indicating stronger aerodynamic loading in this region. After optimization, the area of positive aerodynamic work is significantly reduced, suggesting more favorable energy characteristics.

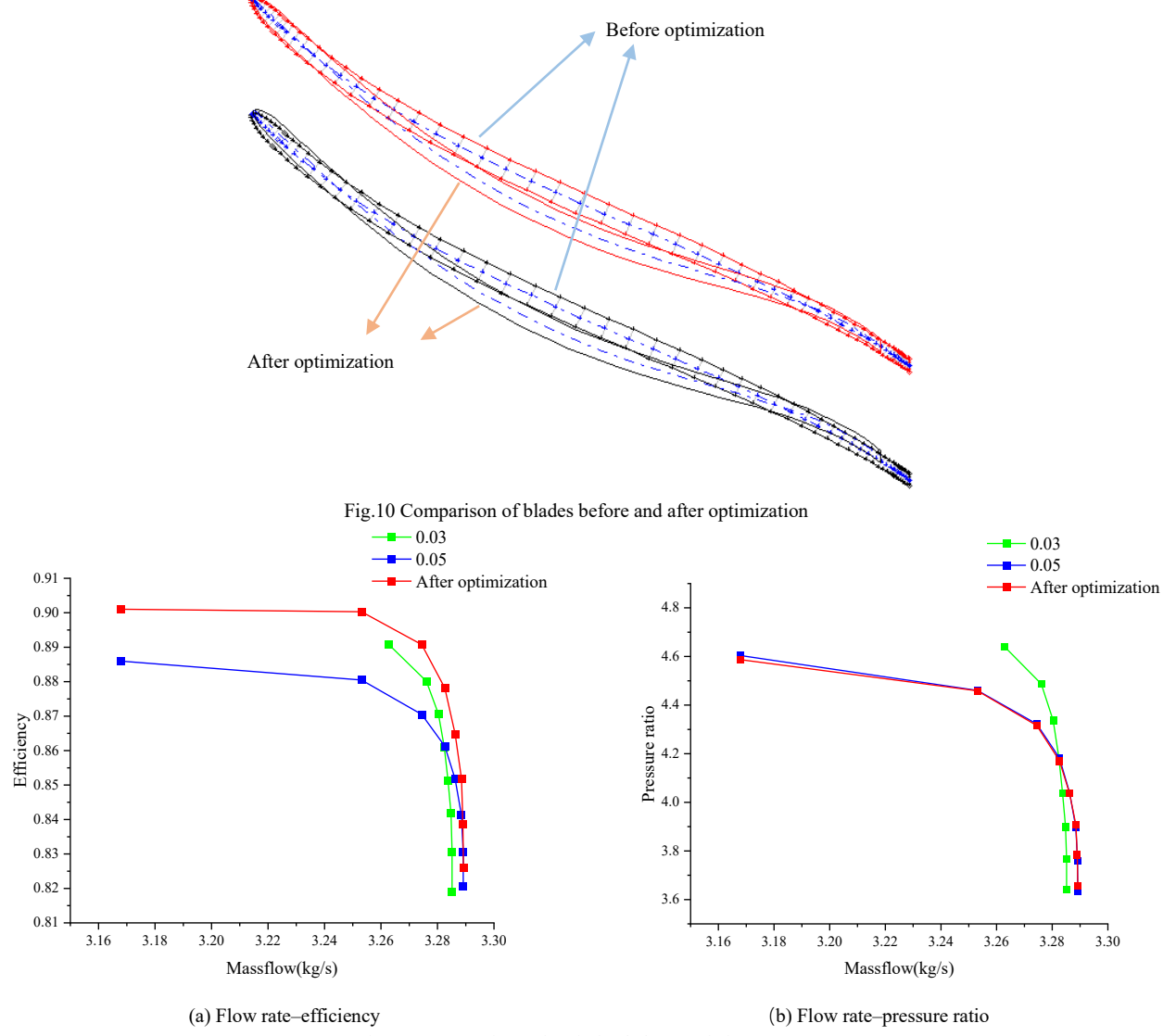


Fig. 11. Comparison of optimized characteristic curves

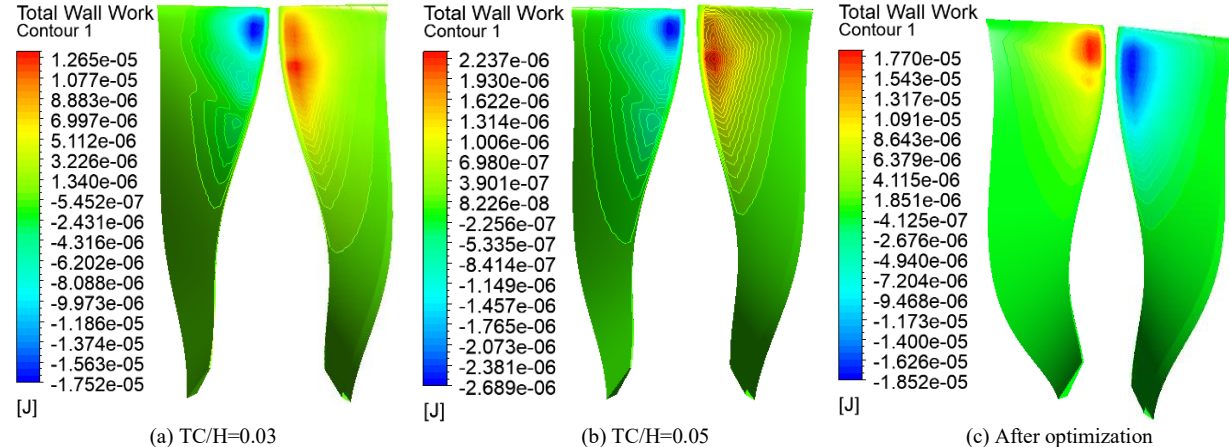


Fig.12 Comparison of aerodynamic work on blade surface before and after optimization (left: suction side; right: pressure side)

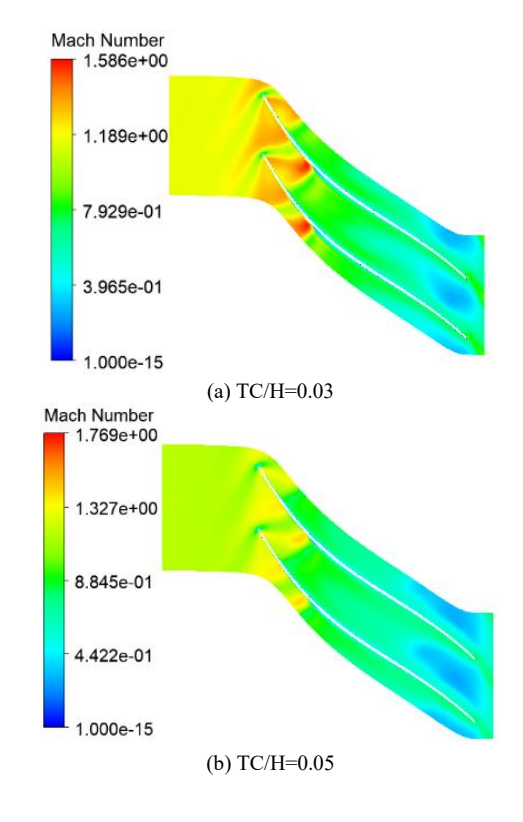
TABLE VIII

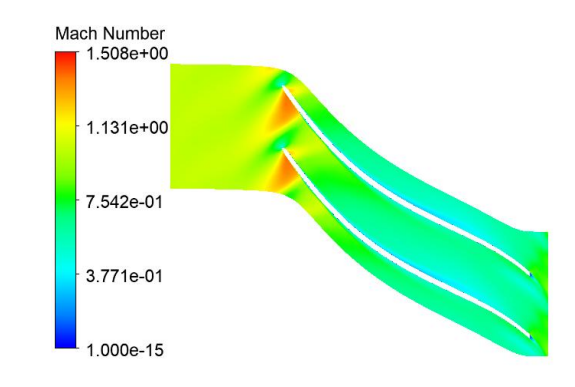
COMPARISON OF AERODYNAMIC WORK AND AERODYNAMIC DAMPING
COEFFICIENT BEFORE AND AFTER OPTIMIZATION

TC/H	Aerodynamic Work (J)	Aerodynamic damping coefficient
0.03	0.000519	0.00103
0.05	0.000102	0.00967
After optimization	-0.00101912	0.0007815

As shown in Table VIII, the aerodynamic work on the blade surface changes from positive to negative after optimization. The optimized impeller exhibits an aerodynamic damping coefficient of 0.0007815 and an aerodynamic work of -0.00101912 J. The positive damping coefficient combined with the negative aerodynamic work indicates that the incoming flow performs negative work on the blade structure as a whole. According to the energy method, a positive aerodynamic damping ratio and negative aerodynamic work both suggest that the blade dissipates energy during vibration, which is beneficial for suppressing flutter and maintaining aeroelastic stability.

## (3) Comparison of Mach Number Before and After Optimization





(c) After optimization
Fig.13 Optimize the Mach number of the front and rear blades

As illustrated in Fig. 13, a comparison between the TC/H ratios of 0.03 and 0.05 reveals that an increase in TC/H leads to more pronounced regions of high local Mach number within the blade passage. These regions are prone to inducing shock waves or flow separation on the suction side, thereby increasing aerodynamic losses and load fluctuations. In contrast, after optimization, the Mach number distribution becomes significantly more uniform, and the peak values are reduced. This indicates that the adverse pressure gradients and vortex structures on the blade surface are effectively suppressed, which not only mitigates the detrimental effects of shock interference on impeller performance but also improves the smoothness of flow within the passage and enhances energy transfer efficiency.

## (4) Comparison of Turbulence Eddy Dissipation Before and After Optimization

The turbulence eddy dissipation rate on the blade surface characterizes the rate at which turbulent kinetic energy is transferred from larger coherent structures to smaller eddies and eventually dissipated into thermal energy due to viscous effects. This parameter provides critical insight into the local turbulence intensity and mixing behavior within the boundary layer and near-wall regions. In particular, high dissipation zones typically coincide with regions of flow separation, vortex shedding, and secondary development, serving as indicators of elevated aerodynamic losses and unsteady flow structures. As such, analyzing the distribution of eddy dissipation on blade surfaces is essential not only for evaluating aerodynamic efficiency but also for assessing the potential onset of aeroelastic instabilities such as flutter.

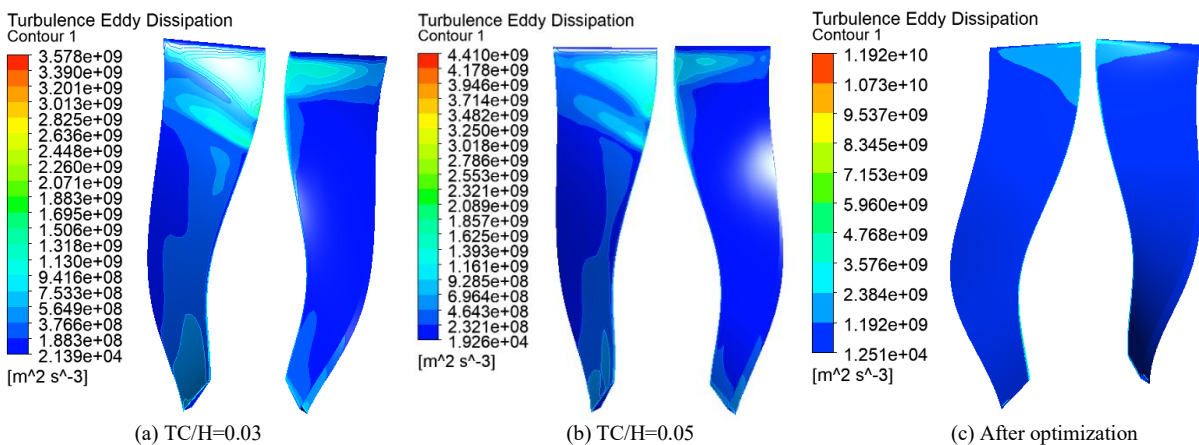


Fig. 14 Optimize the distribution of turbulent eddy dissipation rate of front and rear blades(left: suction side; right: pressure side)

As illustrated in Fig. 14, the distributions of turbulence eddy dissipation on both the suction and pressure surfaces of the blade are compared for three cases: TC/H = 0.03, TC/H = 0.05, and the optimized configuration. The results demonstrate significant variations in both the magnitude and spatial extent of high-dissipation regions as the tip clearance-to-span ratio (TC/H) changes. For TC/H = 0.05, intense dissipation zones are primarily localized near the blade tip and trailing edge, where increased tip leakage and flow separation contribute to greater energy losses and unsteady flow behavior. The enlarged tip clearance promotes leakage vortex formation and intensifies the interaction between primary and secondary flows, thereby amplifying local turbulence and aerodynamic damping reduction.

In contrast, the optimized design exhibits a marked suppression of peak dissipation levels and a more uniform distribution of energy dissipation across the blade surface. The extent of high dissipation regions is notably diminished, indicating a reduction in local flow disturbances and a mitigation of small-scale vortex activity. Particularly in the rear section and tip region, the smoother gradients of dissipation suggest improved boundary layer adherence and a decrease in separated flow zones. These changes reflect a more favorable pressure recovery process and improved flow reattachment dynamics, resulting in enhanced internal flow stability.

#### VI. CONCLUSION

This study conducts a comprehensive investigation into the efficiency and flutter characteristics of centrifugal compressor blades through an integrated approach combining theoretical analysis and numerical simulation. The main conclusions are as follows:

- (1) Flutter analysis based on the traveling wave model and energy method identifies the inter-blade phase angle (IBPA) and aerodynamic damping ratio as critical parameters governing blade aeroelastic stability. Numerical results show that variations in the tip clearance-to-blade height ratio (TC/H) significantly alter the distribution of aerodynamic work and the location of shock waves on the blade surface. These changes substantially influence the aerodynamic energy transfer mechanism, providing a reliable foundation for the quantitative evaluation of flutter risk.
- (2) A multi-objective optimization framework was developed using TC/H along with the blade inlet and outlet

metal angles ( $\beta_1$  and  $\beta_2$ ) as design variables, targeting both aerodynamic efficiency and flutter suppression. The optimized configuration indicates that a moderate TC/H, an increased inlet metal angle, and a suitably tuned outlet angle not only enhance overall compressor efficiency but also reverse the aerodynamic work from positive to negative on the blade surface. This transition effectively mitigates flutter risk and improves the aeroelastic stability of the impeller.

#### REFERENCES

- [1] Shi, Ting, and Xueyuan Peng. "Performance Assessment and Optimiza tion of the Ultra-High Speed Air Compressor in Hydrogen Fuel Cell V ehicles." Applied Sciences 14.3 (2024): 1232.
- [2] Sun, Xilei, et al. "Many-objective optimization for structural paramete rs of the fuel cell air compressor based on the Stacking model under m ultiple operating conditions." *Applied Thermal Engineering* 245 (202 4): 122786.
- [3] Genovese, Matteo, et al. "Integration of hydrogen compressors and turbines into current and future hydrogen infrastructure." *Journal of powe r sources* 629 (2025): 235965.
- [4] Shi, Ting, et al. "Experimental investigation on the start-stop performa nce of gas foil bearings-rotor system in the centrifugal air compressor for hydrogen fuel cell vehicles." *International Journal of Hydrogen En* ergy 48.88 (2023): 34501-34519.
- [5] Ying, Ming, and Xinghua Liu. "Unbalance Response of a Hydrogen F uel Cell Vehicle Air Compressor Rotor Supported by Gas Foil Bearing s: Experimental Study and Analysis." *Lubricants* 13.4 (2025): 181.
- [6] Chen, Fu-qiang, et al. "Propagation study of distorted flow along rotor blades and its impact on blade vibration." Proceedings of the Institutio n of Mechanical Engineers, Part G: Journal of Aerospace Engineerin g (2025): 09544100251328444.
- [7] Gallardo, Juan Manuel, and Óscar Pérez Escobar. "Numerical Study of Low Engine Order Excitations Due to Manufacturing Variability Part II: An Efficient Approach for Stochastic Studies." *Journal of Engineer* ing for Gas Turbines and Power 147.6 (2025).
- [8] Pinelli, L., et al. "Understanding the Aerodynamic Damping Behavior of an Axial Compressor Rotor for Industrial Applications." Proceeding s of the ASME Turbo Expo 2024: Turbomachinery Technical Conferen ce and Exposition. ASME, 2024.
- [9] John R Scheibel, Robert P Dewey, et al., "Gas turbine compressor dependability and risk mitigation measures," in *Proc. ASME Turbo* Expo 2013, GT2013-95143.
- [10] V. V. Vedeneev, M. Kolotnikov, and P. Makarov, "Experimental validation of numerical blade flutter prediction," *J. Propul. Power*, vol. 31, no. 5, pp. 1281–1291, 2015.
- [11] Arshad, Ali, and Akshay Murali. "Aerodynamic Analysis of Blade Stal 1 Flutter Prediction for Transonic Compressor Using Energy Method. " Aerospace 11.10 (2024): 815.
- [12] B. Lakshminarayana, "Methods of predicting the tip clearance effects in axial-flow turbomachinery," *J. Basic Eng.*, vol. 92, no. 3, pp. 467–480, 1970.
- [13] Xin, Jiali, et al. "Influence mechanism of tip clearance on flutt er stability with different aerodynamic coupling effects for tran sonic compressor." *Journal of Physics: Conference Series*. Vol. 2707. No. 1. IOP Publishing, 2024.

- [14] Guo-Rong Gao, Rui-Hui Zeng, and Mei-Ning Chen, "Variation law of tip clearance and its impact on aerodynamic performance in compressors," Sci. Technol. Eng., vol. 24, no. 6, pp. 2573–2580, 2024.
- [15] Zhi-Yuan Liu, "Study on the influence of tip clearance on flow field structure and flutter characteristics in axial compressors," M.S. thesis, Shaanxi Univ. of Technology, Shaanxi, China, 2024.
- [16] Chen-Kai Zhang, Jun Hu, Zhi-Qiang Wang, et al., "Numerical study on tip clearance flow structure of axial compressor rotors," *Acta Aeronaut. Astronaut. Sin.*, vol. 35, no. 5, pp. 1236–1245, 2014.
- [17] J. Micklow and J. Jeffers, Semi-actuator disk theory for compressor chock flutter, NASA Rep. 3426.
- [18] K. Li, Y. Du, Z. Xu, et al., "Flutter analysis of compressor blades under travelling wave modes using an efficient fluid–structure interaction method," *Chin. J. Aeronaut.*, vol. 36, no. 11, pp. 221–232, 2023.
  [19] Yu-Peng Liu, Yong Liu, Yun-Zhu Li, et al., "Flutter prediction of
- [19] Yu-Peng Liu, Yong Liu, Yun-Zhu Li, et al., "Flutter prediction of compressor swept blades using multiple deep learning models," *J. Aero. Power*, pp. 1–11, published online Feb. 18, 2025.
- [20] Yu-Xin Gai and Wan-Heng Kang, "Time-domain method for flutter prediction of large wind turbine blades," *Ind. Metrol.*, vol. 34, no. 3, pp. 5–10, 2024.
- [21] Li-Ping Dai, Xue-Feng Bai, Xiao-Dong Wang, et al., "Prediction and analysis of flutter boundary in large wind turbine blades," *J. Eng. Thermophys.*, vol. 43, no. 9, pp. 2357–2362, 2022.
- [22] Yu-Peng Liu, Yun-Zhu Li, Yu-Xuan Luo, et al., "Effect of radial inflow distortion on blade flutter characteristics of gas turbine compressors," J. Power Eng., vol. 44, no. 9, pp. 1361–1369, 2024.
- [23] Xiang Zhang, Xiu-Quan Huang, Heng-Ming Zhang, et al., "Effect of shock wave on flutter characteristics of transonic fan blades," *J. Propul. Technol.*, vol. 37, no. 3, pp. 411–418, 2016.
- [24] Xiang Zhang, Hai-Yang Wei, Yong-Jie Dang, et al., "Influence of inter-blade coupling on flutter characteristics of transonic compressor rotors," *J. Propul. Technol.*, vol. 44, no. 4, pp. 52–62, 2023.
- [25] X. Duan, J. Cong, Z. Dai, et al., "Influence mechanism and quantificational evaluation of key factors affecting flutter stability of a transonic fan," *Aerosp. Sci. Technol.*, vol. 138, Art. no. 108312, 2023.
- [26] Lane, Frank, and Manfred Friedman. Theoretical investigation of subsonic oscillatory blade-row aerodynamics. No. NACA-TN-4136. 1958

Zhiqiang Dong received the M.S. degree from Dalian University of Technology, Dalian, China, in July 2005. He then transferred to the doctoral program in the School of Energy and Power Engineering ahead of schedule and received the Ph.D. degree in refrigeration and cryogenic engineering from Dalian University of Technology in 2009. He joined Taiyuan University of Science and Technology in 2012, where he is currently an Associate Professor with the School of Vehicle and Transportation Engineering. His research interests include turbomachinery engines, turbocompressors, dynamic and static air bearing technology, intelligent continuous flow microreaction systems, and thermal management of power batteries.

**Genliang Yu** is currently pursuing the M.S. degree in vehicle engineering at the School of Vehicle and Transportation Engineering, Taiyuan University of Science and Technology, Taiyuan, China. His research interests include lightweight and integrated technologies for construction machinery and electric vehicles, and turbocompressor design and optimization.